Crustal structure of the propagating TAMMAR ridge segment on the Mid-Atlantic Ridge, 21.5°N

Anke Dannowski, Ingo Grevemeyer, J.Phipps Morgan, C.R. Ranero, Marcia Maia, G. Klein

Geochemistry Geophysics Geosystems G3

Article
Volume 12, Number 7
19 July 2011
Q07012, doi:10.1029/2011GC003534
ISSN: 1525-2027

Published by AGU and the Geochemical Society

Crustal structure of the propagating TAMMAR ridge segment on the Mid-Atlantic Ridge, 21.5°N

A. Dannowski and I. Grevemeyer
Leibniz-Institut für Meereswissenschaften an der Universität Kiel (IFM-GEOMAR), Wischhofstrasse 1-3, D-24148 Kiel, Germany (adannowski@ifm-geomar.de)

J. Phipps Morgan
Department of Geology, Cornell University, Ithaca, New York 14853, USA

C. R. Ranero
ICREA, Barcelona Center for Subsurface Imaging, Institut de Ciencias del Mar, CSIC, Pg. Marítim de la Barceloneta 37-49, E-08003 Barcelona, Spain

M. Maia
Université Européenne de Bretagne, F-35000 Rennes, France

Laboratoire Domaines Océaniques, CNRS-Université de Brest, IUEM, Rue Dumont d'Urville, F-29280 Plouzané, France

G. Klein
Leibniz-Institut für Meereswissenschaften an der Universität Kiel (IFM-GEOMAR), Wischhofstrasse 1-3, D-24148 Kiel, Germany

[1] Active ridge propagation frequently occurs along spreading ridges and profoundly affects ridge crest segmentation over time. The mechanisms controlling ridge propagation, however, are poorly understood. At the slow spreading Mid-Atlantic Ridge at 21.5°N a seismic refraction and wide-angle reflection profile surveyed the crustal structure along a segment controlled by rapid ridge propagation. Tomographic traveltime inversion of seismic data suggests that the crustal structure along the ridge axis is controlled by melt supply; thus, crust is thickest, 8 km, at the domed segment center and decreases in thickness toward both segment ends. However, thicker crust is formed in the direction of ridge propagation, suggesting that melt is preferentially transferred toward the propagating ridge tip. Further, while seismic layer 2 remains constant along axis, seismic layer 3 shows profound changes in thickness, governing variations in total crustal thickness. This feature supports mantle upwelling at the segment center. Thus, fluid basaltic melt is redistributed easily laterally, while more viscose gabbroic melt tends to crystallize and accrete nearer to the locus of melt supply. The onset of propagation seems to have coincided with the formation of thicker crust, suggesting that propagation initiation might be due to changes in the melt supply. After a rapid initiation a continuous process of propagation was established. The propagation rate seems to be controlled by the amount of magma that reaches the segment ends. The strength of upwelling may govern the evolution of ridge segments and hence ultimately controls the propagation length.

Components: 10,300 words, 8 figures.

Keywords: crustal structure; mid-ocean ridges; ridge propagation; seismic traveltime tomography.

Index Terms: 3025 Marine Geology and Geophysics: Marine seismics (0935, 7294); 3035 Marine Geology and Geophysics: Midocean ridge processes; 8416 Volcanology: Mid-oceanic ridge processes (1032, 3614).

Received 28 January 2011; **Revised** 25 May 2011; **Accepted** 25 May 2011; **Published** 19 July 2011.

Dannowski, A., I. Grevemeyer, J. Phipps Morgan, C. R. Ranero, M. Maia, and G. Klein (2011), Crustal structure of the propagating TAMMAR ridge segment on the Mid-Atlantic Ridge, 21.5°N, *Geochem. Geophys. Geosyst.*, *12*, Q07012, doi:10.1029/2011GC003534.

1. Introduction

[2] Mid-ocean ridges exhibit different types and scales of segmentation [*MacDonald et al.*, 1988] that can be classified according to their shape, size and longevity. Crustal accretion at the Mid-Atlantic Ridge (MAR) appears to be complex, is not uniform along axis, and is viewed as a focused and three-dimensional process [*Lin et al.*, 1990; *Lin and Phipps Morgan*, 1992; *Tolstoy et al.*, 1993; *Magde and Sparks*, 1997]. The typical segment length at the slow spreading northern MAR is generally less than 100 km [*Sempéré et al.*, 1993; *Smith et al.*, 2003]. However, the segment length may vary through time [*Gente et al.*, 1995; *Gac et al.*, 2006] and some segments lengthen at the expense of their neighbors, leaving oblique structures created by this ridge propagation.

[3] The mechanisms driving rift propagation are still poorly understood. Several nonexclusive and variable quantified potential mechanisms have been proposed to describe active propagating ridges (PR), including propagation down an along-ridge axis topographic gradient [*Phipps Morgan and Parmentier*, 1985; *Phipps Morgan and Sandwell*, 1994], changes in direction of seafloor spreading [*Wilson et al.*, 1984; *Hey et al.*, 1980, 1988; *Briais et al.*, 2002], a crack propagation force [*MacDonald et al.*, 1991], hot spots [*Schouten et al.*, 1987; *Brozena and White*, 1990], and tectonic extension due to changes in the magmatic period [*Kleinrock and Tucholke*, 1997].

[4] Active propagating ridges have been detected at all types of ridges, from slow to fast spreading rates and at large and small scales. They have been investigated, for instance, at the Galapagos spreading center [e.g., *Hey et al.*, 1980], the Juan de Fuca Ridge [e.g., *Hey*, 1977] (both intermediate spreading rates), the East Pacific Rise [e.g., *Hey et al.*, 1986; *Cormier and MacDonald*, 1994] (fast spreading center), the Pacific-Antarctic Ridge [*Briais et al.*, 2002], and the Mid-Atlantic Ridge [e.g., *Carbotte et al.*, 1991; *Sempéré et al.*, 1995; *Kleinrock and Tucholke*, 1997] (as an example of slow spreading ridges). Propagation rates appear to depend on the spreading rate of the ridge segments; thus, the higher the spreading rate at the ridge, the higher the propagation rate [*Phipps Morgan and Sandwell*, 1994].

[5] At 21°30′N a propagating ridge segment, the TAMMAR segment (Figure 1), occurs at the slow spreading Mid-Atlantic Ridge (MAR) [*Gente et al.*, 1995]. The off-axis trace left by the propagator in the last 5 million years can be easily traced even in satellite altimetry-derived gravity data [*Sandwell and Smith*, 1997]. The evolution of the propagating ridge segment is expected to be connected to temporal variations in crustal production, as derived from gravity field data [*Maia and Gente*, 1998]. Earlier seismic refraction studies from other "hourglass" shaped segments along the MAR were published at 5°S [*Planert et al.*, 2009], at 33°S [*Tolstoy et al.*, 1993], and at the OH-1 segment at 35°N [*Hooft et al.*, 2000; *Canales et al.*, 2000]. In comparison all four segments have lots of similarities; however, in our study area a transform fault (TF) stable for several million years did not stop segment propagation. The TAMMAR segment propagates through the southern transform offset instead of through the zero-offset discontinuity to the north. In this study, we present seismic data from the TAMMAR segment that were acquired from R/V *Meteor* (M60/2) in December 2003 and January 2004. We report constraints on the melt supply and melt distribution during ridge propagation using seismic refraction and wide-angle reflection data (Figure 1a).

2. Tectonic Settings

[6] The TAMMAR segment at 21.5°N on the MAR is thought to be one of the most magmatic segments of the MAR [*Gente et al.*, 1995; *Thibaud et al.*, 1998] and has propagated southward (Figure 1b). The segment has a length of about 90 km and shows smooth variations in axial valley morphology from the segment center toward the segment ends. For a slow spreading ridge, like the MAR, the PR displays a remarkably fast rate, propagating at a rate roughly 0.6 times the spreading rate. This PR began its southward propagation approx. 4.5 million years ago [*Gente et al.*, 1995], propagating through a transform offset to the south, producing a V-shaped wake in the lithosphere (Figure 1a). At the OH-1 segment propagation started roughly 5 million years ago and propagated away from the large-offset Oceanographer fracture zone [*Rabain et al.*, 2001].

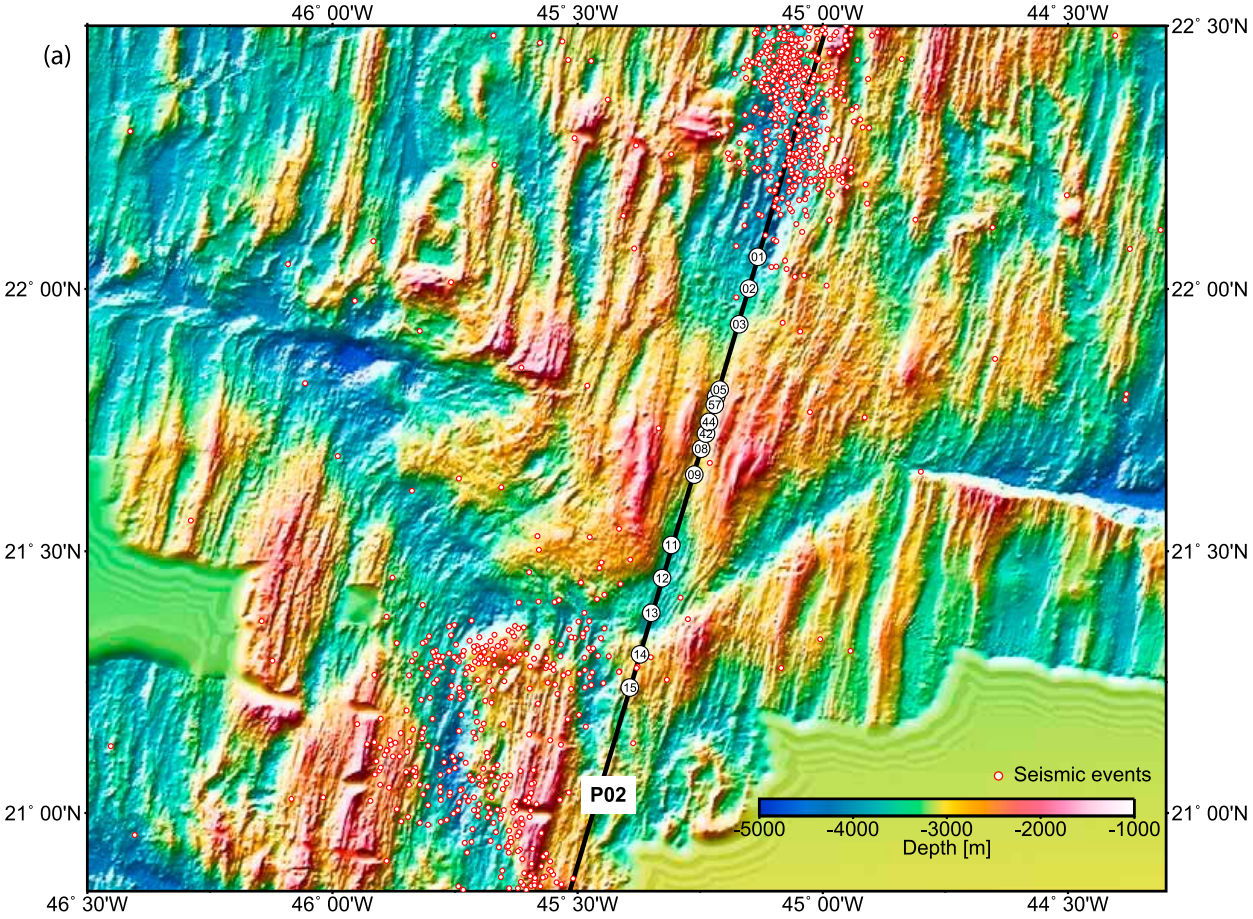
(a)
46° 00'W
45° 30'W
45° 00'W
44° 30'W
22° 30'N
22° 00'N
21° 30'N
21° 00'N
46° 30'W
01
02
03
05
57
44
42
08
09
11
12
13
14
15
P02
Seismic events
-5000
-4000
-3000
-2000
-1000
Depth [m]

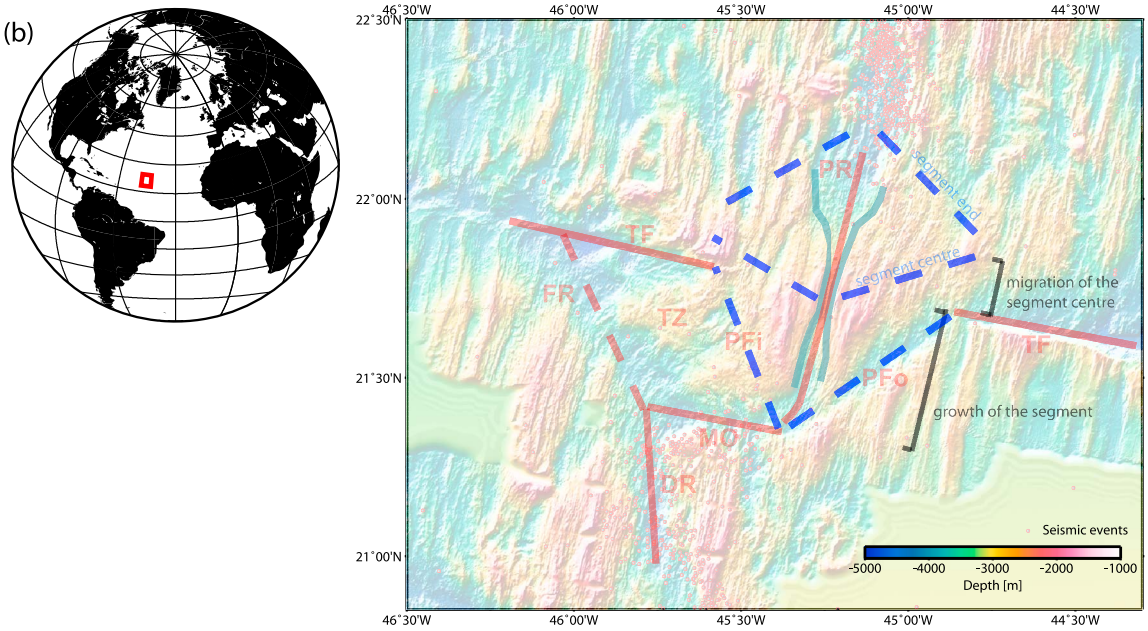
(b)
46°30'W
46°00'W
45°30'W
45°00'W
44°30'W
22°30'N
22°00'N
21°30'N
21°00'N
PR
segment end
TF
segment centre
migration of the segment centre
FR
TZ
PFi
PFo
TF
growth of the segment
MO
DR
Seismic events
-5000
-4000
-3000
-2000
-1000
Depth [m]

Figure 1

The process of rift propagation generally involves the lengthening of the spreading segment at the expense of the adjacent segments [*Gente et al.*, 1995].

[7] A detailed model of ridge propagation was given by *Hey et al.* [1980] and *McKenzie* [1986] assuming that the PR extends at a constant rate. Figure 1b describes the propagation tectonics for the studied area geometrically. The northern segment end is a zero-offset discontinuity at 22°05′N. The southern segment boundary corresponds to a 40 km long offset at 21°20′N, the migrated offset (MO). A second ridge-normal feature at 21°40′N is a fossil transform fault (TF). The continuous structures of the ancient fault zone illustrate the stability of this spreading segment over the time before propagation started [*Gente et al.*, 1995]. However, at the early stages of the propagation, this setting became instable and the structures disappear near the ridge axis. A continuous V-shaped trace connects the ancient now inactive transform with the present offset feature. During propagation the present-day axial discontinuity has shortened in offset from about 50 km to its present-day 40 km. It may no longer be a TF, but instead is a "sheared zone." The propagating ridge (PR) takes over the role of spreading from its southern neighbor known as doomed ridge (DR). It leaves behind a characteristic footprint in the shape of a V. While the eastern trace, outer pseudofault (PFo), is an elongate narrow depression, the western trace, the failed ridge (FR) and the inner pseudofault (PFi), is a tectonically wide disturbed area which characterizes the patch of transferred lithosphere (TZ) during the propagation (Figure 1b). The doomed ridge appears as an asymmetric oblique structure, the ridge axis steps eastward from north to south.

[8] The linear wake was created by a constant propagation rate of approx. 16 mm/y after a rapid initiation of propagation [*Phipps Morgan and Sandwell*, 1994], while the spreading rate has remained constant [*DeMets et al.*, 1990]. Knowing the half-spreading rate v from magnetic anomalies, the propagation rate p can be estimated by measuring the acute angle θ between the propagating ridge and a pseudofault [*Kleinrock and Tucholke*, 1997]: $p = v/\tan\theta$ (Figure 1b). The PR has slightly asymmetric accretion with an average half spreading rate of 14 mm/y on the western flank compared to 12 mm/y on the eastern flank [*Maia and Gente*, 1998].

[9] PR driving forces were strong enough to "cut" the transform at 21°40′N and force its migration to the south. The bathymetric V-shaped structure corresponds to a large mantle Bouguer anomaly of −40 mGal and thus, is one of the largest anomalies along the MAR [*Maia and Gente*, 1998]. PRs along the MAR for example at 33°S [*Tolstoy et al.*, 1993] or 35°N [*Hooft et al.*, 2000] showed similar large mantle Bouguer anomalies, however, propagation stopped at transform faults.

[10] A general feature of propagating ridge segments along the northern MAR is the southward trend of all propagating segments between 26°30′N and the Azores hot spot. However, south of 26°30′N they have randomly propagated both north and south, splitting the ridge flanks into rhomb-shaped areas [*Gente et al.*, 1995]. Mantle rocks have been found at the northern terminus of the propagating segment. This may be linked to amagmatic extension in a magmatically starved setting [*Dannowski et al.*, 2010].

[11] The TAMMAR segment shows an hourglass shaped axial valley morphology that change from the segment center toward the segment ends. At 21°47′N the shallowest on-axis area of the segment is 2 km wide and ~3 km deep with walls ~600 m high. During a submersible study [*Gente et al.*, 1996], two types of volcanism were identified on the inner floor: Isolated volcanoes and piled lava flows, flat lava lakes. They found that the isolated volcanoes are 500 m to 1000 m in diameter and consist mainly of pillow lavas and lava tubes on the steeper slopes. Most of the inner valley is covered by flat areas, lava lakes up to 7 m deep, which indicate high volcanic effusion rates [*Gente et al.*, 1996]. Seafloor volcanism is focused at the center and sparse at the tip of the segment. At the southern end of the segment the inner floor of the axial valley is 4–5 km wide and 3.5 km deep on average. Volcanism is represented only by isolated pillow lava volcanoes. The freshest basalts are in the deepest part of the inner floor as in other parts of the segment. The northern segment end is characterized by a 15 km wide and 4 km deep basin, indicating lower magmatism.

3. Seismicity of the Segment

[12] A hydroacoustic experiment along the MAR was performed by NOAA's Pacific Marine Envi-

Figure 1. (a) Map of the study area. The heavy line represents the shot profile. White circles with numbers indicate the distribution of instruments in this study along profile P02. Red circles with white background represent the hydroacoustically detected events reported by the PMEL [*Smith et al.*, 2003]. (b) The tectonic interpretation of the seafloor in the study area, explained in the text.

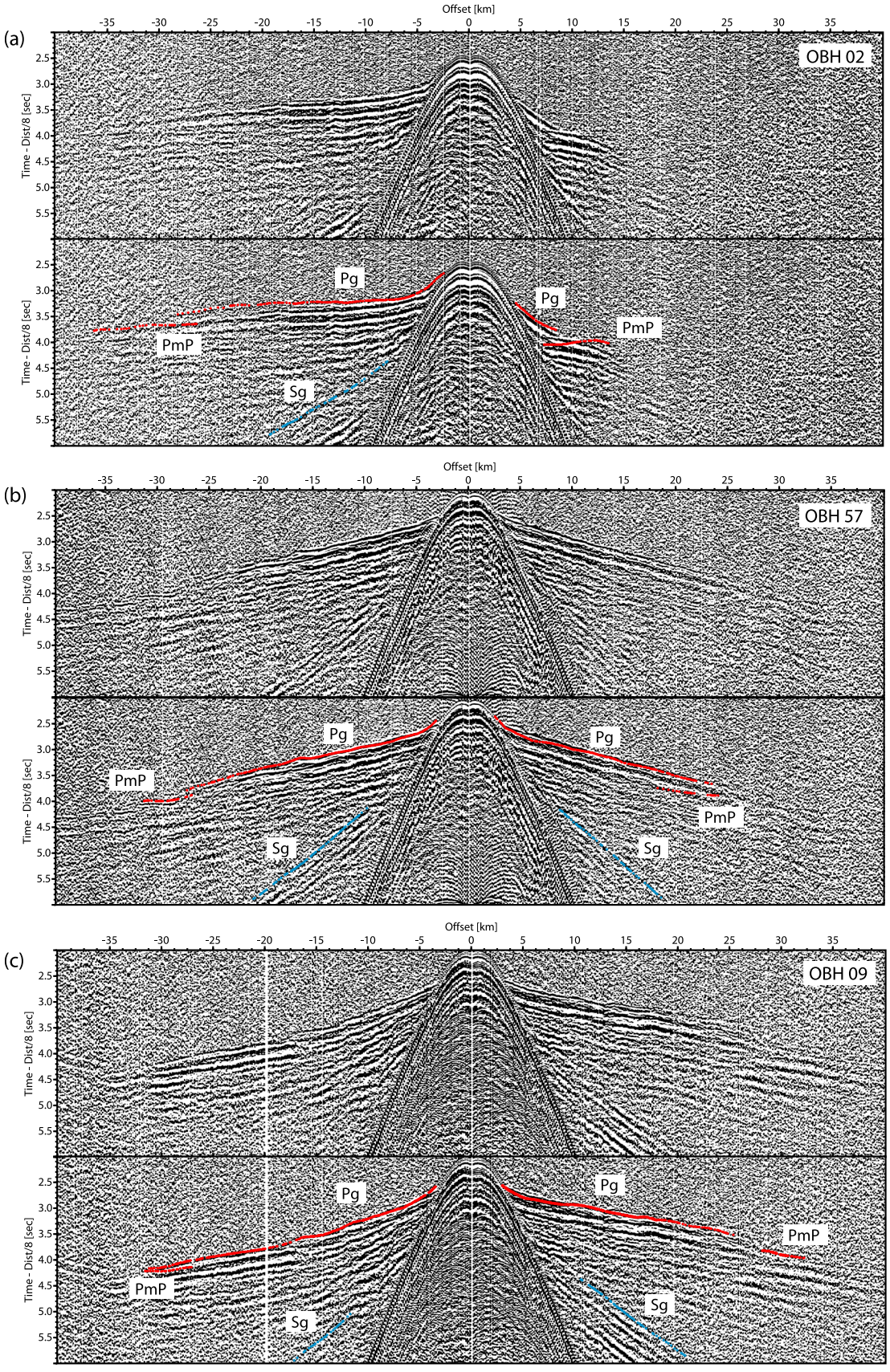
(a)
OBH 02
Offset [km]
Time - Dist/8 [sec]
Pg
Pg
PmP
PmP
Sg
(b)
OBH 57
Offset [km]
Time - Dist/8 [sec]
Pg
Pg
PmP
PmP
Sg
Sg
(c)
OBH 09
Offset [km]
Time - Dist/8 [sec]
Pg
Pg
PmP
PmP
Sg
Sg

Figure 2

ronmental Laboratory (PMEL) from 1999 to 2001 [*Smith et al.*, 2003]. For a period of ~2 years, six hydrophones were placed on the flanks of the MAR between 15°N and 35°N. Our study area lies between the four southern hydrophones. Hydroacoustically detected events have a lower detection threshold than global seismic networks and report earthquakes with magnitudes of M > 3. The seismic activity reported by PMEL decreases toward the center of the TAMMAR segment (Figure 1a) suggesting thin lithosphere at the segment center and thick lithosphere at the segment ends. The northern deeper part of the ridge axis and the southern segment end show a higher seismicity. Although there is no identifiable offset in the ridge axis, the northern segment boundary is located where seismicity abruptly starts.

[13] The hydroacoustic data showed the gap in seismicity even for small magnitudes [*Smith et al.*, 2003]. The seismicity pattern from the hydroacoustic experiment in this region is consistent with the small number of teleseismic events compared to other segments. Most of the teleseismic events at the MAR are tectonic in origin [*Bergman and Solomon*, 1990] and the volcanic earthquakes on the MAR probably fall below the magnitude threshold for teleseismic detection using global seismic networks. The seismic activity can be used to assess the thermal state of the segment. It indicates that the TAMMAR segment is in a phase of magmatic dominated crustal accretion.

[14] Observations of the southern ridge tip and the migrated offset of the TAMMAR segment are consistent with the hydroacoustic experiment. A seismologic network covered this region with a 6 month deployment of ocean bottom seismometers [*Kahle*, 2007]. While the transform zone and the doomed ridge exhibit strong seismicity, only few events were observed on the propagating ridge and were related to magmatic spreading.

4. Seismic Data Acquisition, Processing, and Analysis

[15] The surveyed area is located between 21 and 22.5°N and 44–46°W (Figure 1). As part of the COSTMAR project an active seismic refraction and wide-angle experiment was carried out including 15 ocean bottom hydrophone (OBH) deployments in a profile along the ridge axis. The 190 km long profile P02 follows the median valley (N-S direction). The topography in this area is rugged even along the ridge axis. The quality of the data is good to excellent (Figure 2); providing clear crustal refraction branches (Pg), crust-mantle boundary (Moho) reflections (PmP), and a few mantle refraction phases (Pn). Converted shear wave arrivals (Sg) are visible at stations in the central portion of the segment. A remarkable number of instruments concentrated at the segment center, did not work properly. This was "corrected" during the expedition by reshooting the central part of the profile in profile P06. For the modeling both profiles have been merged. Picks from OBH42, OBH44, OBH57, and OBH60 could be added to the original profile P02, filling the gap (Figure 1a).

4.1. Data Input and Processing

[16] As source we used two 32-L BOLT Inc. air guns towed in a depth of 5 m, firing 2228 shots (P02: 1550; P06: 678) successfully at a shot interval of 60 s over the two profiles. With an average ship velocity of 4 knots, this yields a trace spacing of approximately 120 m.

[17] Based on GPS and ship's navigation system shot locations were corrected for the offset between the GPS antenna and the air gun array. Receiver positions on the seafloor were relocated using direct water wave traveltimes. All data loggers were synchronized with a GPS time signal to correct for a possible linear clock drift. The data were continuously recorded with a sampling rate of 200 or 250 Hz on all OBH stations. After recovery the data were played back and split into single shot records as a receiver gather in SEG-Y format. To enhance the signal-to-noise ratio we applied statistical deconvolution in time windows, amplitude balance, and an Ormsby frequency filter. The time- and offset-variant band-pass filter moves toward lower frequencies as time and offset increase. Data examples are given in Figure 2.

Figure 2. Hydrophone records of reduced velocity to 8 km/s for selected instruments of P02. The top plot for each section shows processed data, and the bottom plot for each section shows calculated picks after the traveltime tomography (red dots for P wave and blue dots for S wave tomographic results): (a) OBH02, (b) OBH57, (c) OBH09, (d) OBH11, and (e) OBH14. Phases are labeled as follows: Pg, refracted crustal arrival; PmP, reflected mantle arrival; Sg, refracted crustal P-to-S converted phase arrival. (f) Images of the raypaths for P wave traveltimes of three stations through the preferred model.

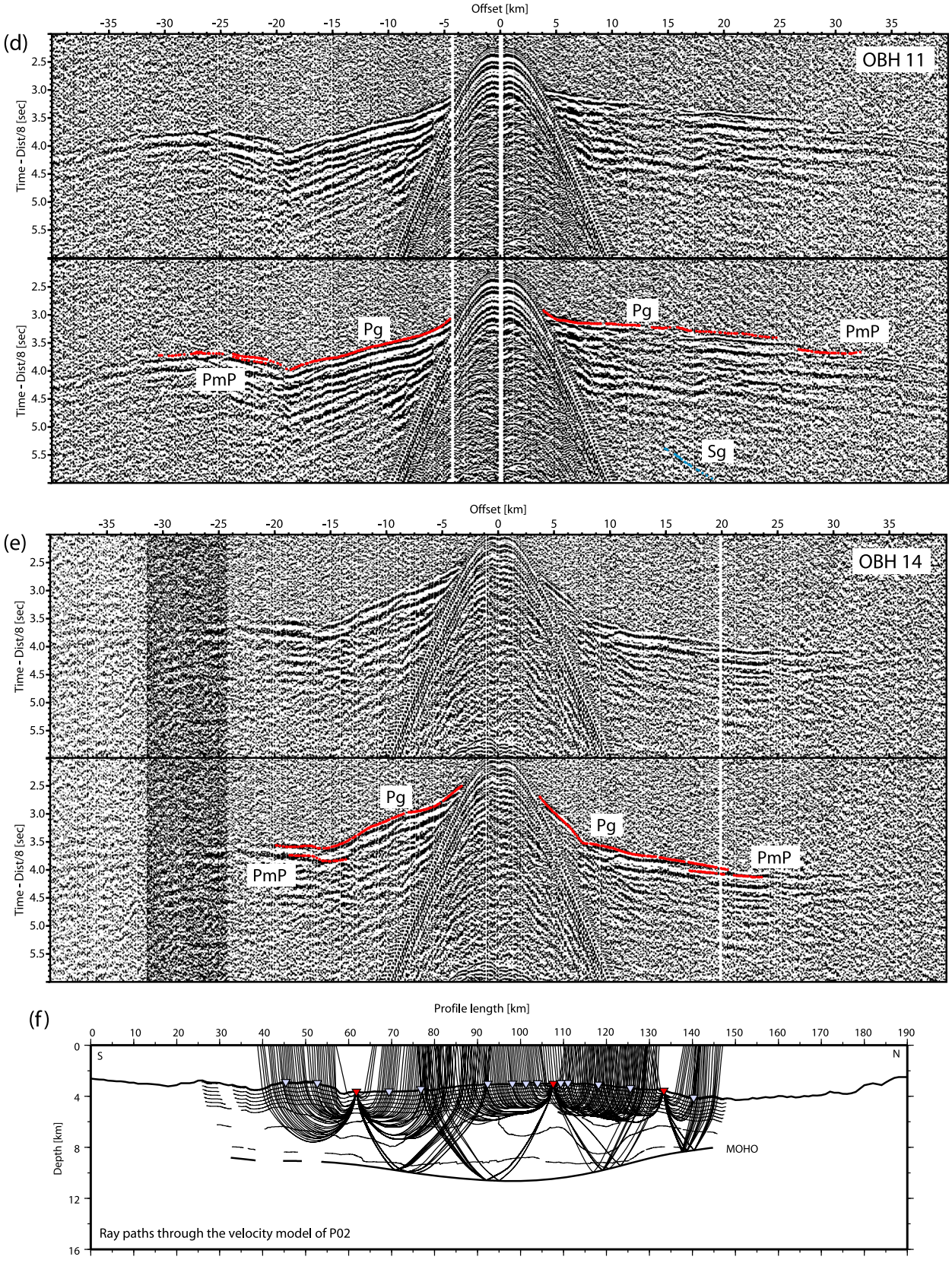

Figure 2. (continued)

4.2. Traveltime Picking

[18] Most of the stations show a high signal-to-noise ratio that allowed clear identification of P wave arrivals. Three distinct crustal arrivals were identified: a high-amplitude refracted phase from layer 2 that occurs to ranges of ~15 km (Pg); a lower-amplitude refracted phase from layer 3 that continues to ranges of up to 35 km (Pg); and a high-amplitude wide-angle reflection from the crust-mantle boundary (Moho) observed on some stations as a distinct second arrival at 20–40 km range (PmP). We could observe a few refracted mantle phases (Pn) even at large offsets of up to 70 km, partly limited by the profile length. Primary phases at the onset of the first positive amplitude peak from the crust and the mantle and secondary arrivals had been picked manually. Data from five stations are presented in the seismic sections (Figure 2), including OBH02, OBH57, OBH09, OBH11, and OBH14. The pick uncertainty has been estimated ranging from 10 to 70 ms. Larger uncertainties were assigned to noisier data, usually for crustal arrivals with smaller amplitudes recorded at larger source-receiver offsets.

[19] It is interesting to note that the data are strongly affected by the steep bathymetry which obscures PmP arrivals; thus, the PmP phase does not appear on all stations as a clear arrival with strong amplitudes. This feature is perhaps also caused by variation in the velocity contrast at the crust-mantle boundary. Short sections of PmP arrivals were identified and picked where possible. They could be consistently identified using the forward and back shots and the multiples at adjacent stations. The critical distance shows a strong variation along the profile. The offset where the critical distance can be recognized ranges from 10 km in the north to 35 km in the segment center. Thus, northern stations show high velocities interpreted as mantle phases at small offsets (~10 km), while at the segment center mantle phases occur at much larger offsets.

4.3. Traveltime Inversion and Modeling Strategy

[20] The P wave velocity model was determined using the traveltime inversion technique of *Korenaga et al.* [2000], which jointly inverts refracted and wide-angle reflected traveltimes for a two-dimensional velocity structure. The geometry of the Moho is constrained as a floating reflector. To achieve an accurate forward solution the hybrid ray-tracing scheme is based on the graph method [*Moser*, 1991] and additional local ray-bending refinement [*Moser et al.*, 1992] was employed; smoothing and damping constraints were used to regularize the iterative inversion. The velocity model was parameterized as a sheared mesh with parallelogram shaped cells hanging beneath the seafloor. The velocity field is continuous everywhere and is interpolated within each cell. The seafloor was parameterized at a spacing of 1 km while the regular grid has grid cells with a uniform horizontal spacing of 200 m and a vertical increasing spacing from 50 to 170 m. The velocity and depth smoothing and damping parameters were kept the same for all three profiles with 40 and 20 for velocity and depth, respectively. A weighting factor of w = 1 was used for weighting the depth and the velocity nodes equally. A larger weighting factor should lead to larger depth perturbations [*Korenaga et al.*, 2000].

[21] The modeling approach consisted of several steps. First 1-D modeling of single stations from the ends and the center of the profile was performed to derive initial two-dimensional velocity models. Then downward stripping of the layers was carried out by first inverting for the upper crustal arrivals and then inverting for all deeper crustal arrivals. Once found, the upper part of the model was fixed and the first arrival picks of larger offsets were added. In the next step the Moho depth was determined from the PmP arrivals. During each stage a broad model space was tested to verify the model uncertainties. The influence of starting model variations, pick errors, and the reliability of the model was analyzed using synthetic tests and statistical calculations.

5. Results

5.1. P Wave Arrival Tomography

[22] The tomographically determined velocity model of profile 2 (Figure 3) shows up to 4 km of variation in crustal thickness along the ridge axis. In agreement with PmP arrivals, the crustal thickness decreases from 8 km in the segment center to 4 km in the northern segment end. The southern ridge tip has a 5.5 km thick crust which is 1.5 km thicker compared to the northern segment end. The main compensation of the topography is done in layer 3 while layer 2 almost follows the ocean floor topography. Generally, the upper crust has a high velocity gradient (about 1.6 s^{-1}) with velocities increasing from 2.7 km/s at the seafloor to 6.4 km/s at the upper to lower crustal boundary. The average thickness of the upper crust is about 1.8 km. The near-seafloor velocities decrease from the segment center toward the segment ends (3.2–2.7 km/s). The

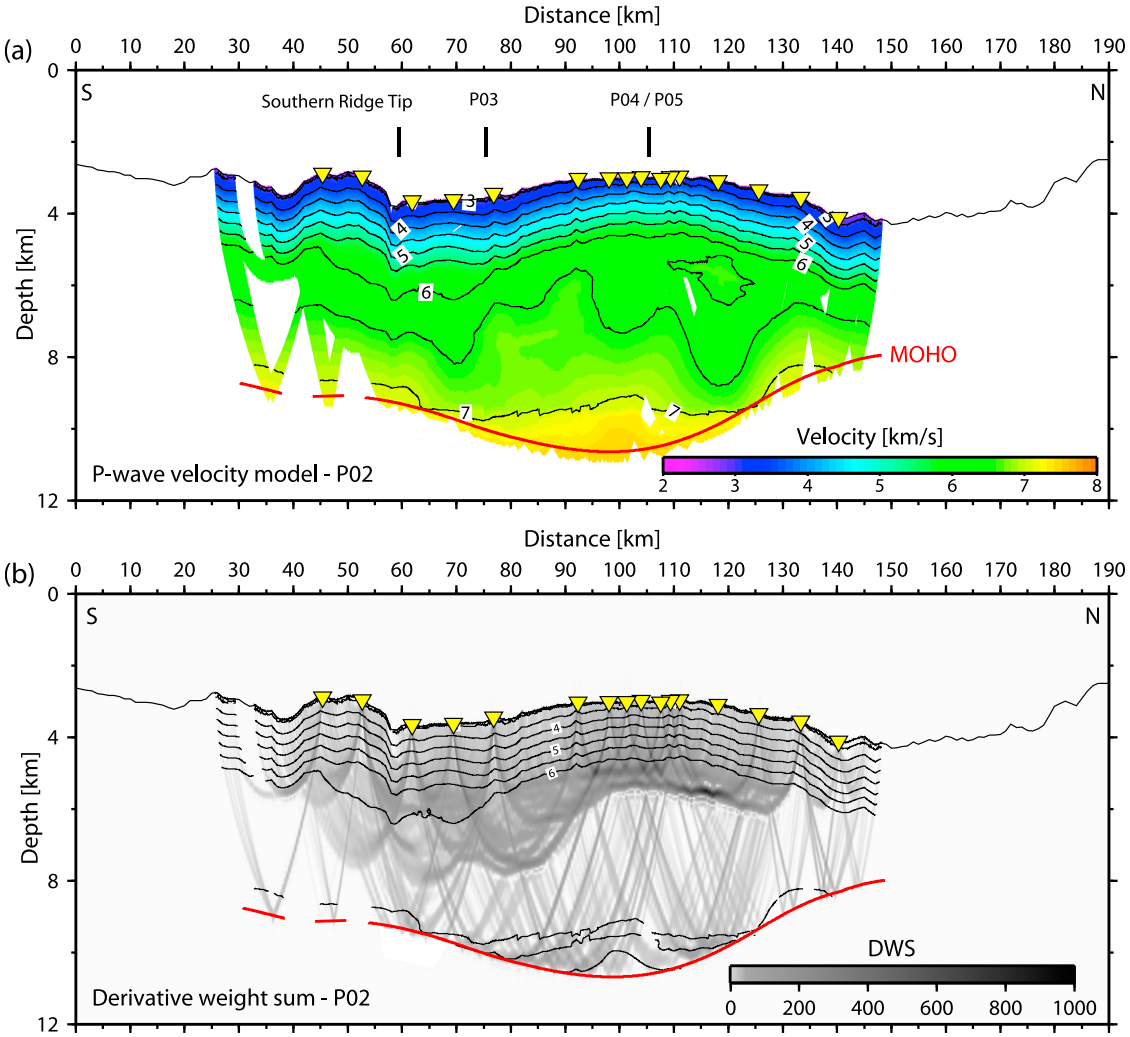

Figure 3. Profile 2: (a) Preferred final P wave velocity model after five iterations. The interval of the contour lines is 0.5 km/s. (b) Resolution of the model and the ray coverage of the tomographic inversion. The interval of contour lines for velocities larger than 7 km/s is 0.2 km/s.

southern ridge tip shows slightly slower upper crustal velocities. The velocity gradient changes suddenly to less than 1 s^{-1} near the layer2/3 boundary. Layer 3 varies from about 2 km to 6 km with velocities increasing from 6.5 km/s to 7.1 km/s in depth. Even higher velocities (larger than 7.2 km/s and up to 7.4 km/s) were observed at the bottom of the segment center.

[23] The detected different offsets of the PmP arrivals (Figure 2) are the result of variations in crustal thickness. This supports results by *Maia and Gente* [1998], who found with gravity data that the segment centers are associated with crustal thickening while depressions are marked by bands of thin crust. Figure 3a shows the reflector (red line) at a depth of 10.5 km to 8 km below sea surface which has been interpreted as the depth of the Moho. Tests of different starting models (high and low constant gradients as well as variations in the depth of the Moho) and changes in the smoothing and damping factors of the inversion program showed that the final model is robust. Starting models with a deeper instead of a shallow Moho provided faster convergence and better fits. In parts covered by stations a standard deviation of 0.1 km/s was reached. In deeper parts and toward the end of the profile the standard deviation becomes larger, about 0.2 km/s in deeper portions of model and up to 0.4 km/s at distances larger than 25 km away from the last station. This means that the velocity model beneath the stations is robust and nearly independent on the starting model, however, at other parts strongly depend on the starting model.

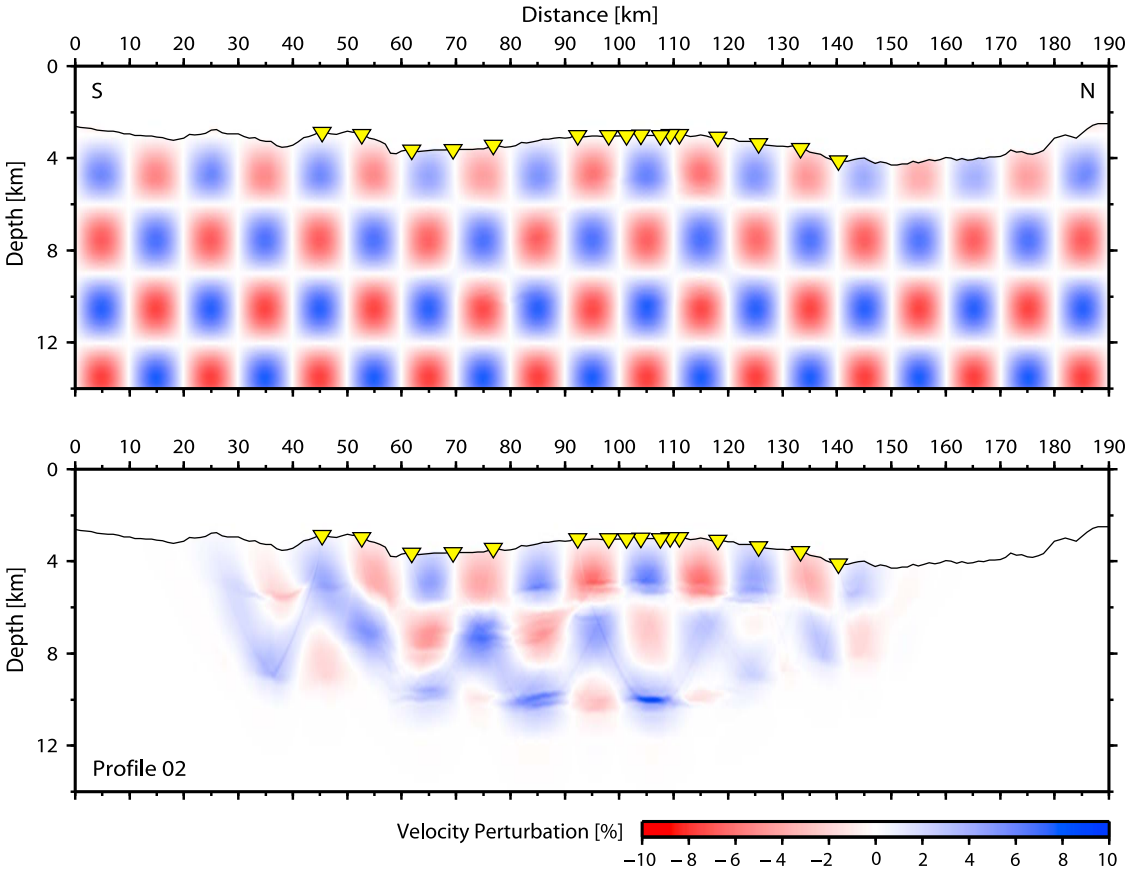

Figure 4. Resolution test (checkerboard test) for the P wave tomographic modeling: (top) The initial perturbations for plus and minus 0.5 km/s. (bottom) The reproduced perturbations. Blue is a negative anomaly, and red is a positive one.

[24] A total of 3883 P wave arrival times could be picked, including 3379 crustal arrivals and 504 mantle reflections. The model evolved after 8 iterations to $X^2 = 1.45$ and a misfit of 72 ms. The ray coverage, expressed by the derivative weight sum (DWS), is good in the central part and poor toward the model boundaries. The results show good correlation between model resolution as inferred from the DWS (Figure 3b) and the checkerboard test (Figure 4). The resolution is good at shallow depths and decreases with increasing depth. The horizontal resolution at shallow depth is estimated as 2.5–5 km based on the recovery of the anomaly pattern in the checkerboard tests. The checkerboard test presented in Figure 4 shows an estimated horizontal resolution of about 10 km for the deeper model portions. Figure 2 shows the calculated traveltime picks for five stations.

5.2. Converted Shear Wave Tomography

[25] Along P02 prominent shear wave energy was observed (Figure 2) on OBHs deployed at the segment center. Recorded S_V waves were generated by P-to-S conversion since a shallow acoustic source was used. In general, shear wave conversion in marine environments occurs at the sediment-basement interface. However, conversion may occur at the seafloor if the S wave velocity of the basement is larger than approximately 1.6 km/s.

[26] Strongest energy was found at offsets of 10 to 25 km at stations OBH03 to OBH11, where P wave velocities are slightly higher than at the segment ends. This may suggest an area of higher density and less fracturing, that enhances conversion. In addition, faster P wave velocity favors faster S wave velocity, again supporting conversion. Therefore, the shear wave velocity of layer 2 is larger than the compressional wave velocity of the water (needed for conversion at the seafloor). The center of the segment shows a P wave velocity of $v_P = 3.2$ km/s. Assuming v_P/v_S is 1.8 this results in $v_S = 1.77$ km/s.

[27] Strong S wave arrivals could be identified on source gathers recorded at stations located from 70 km to about 140 km distance along the profile,

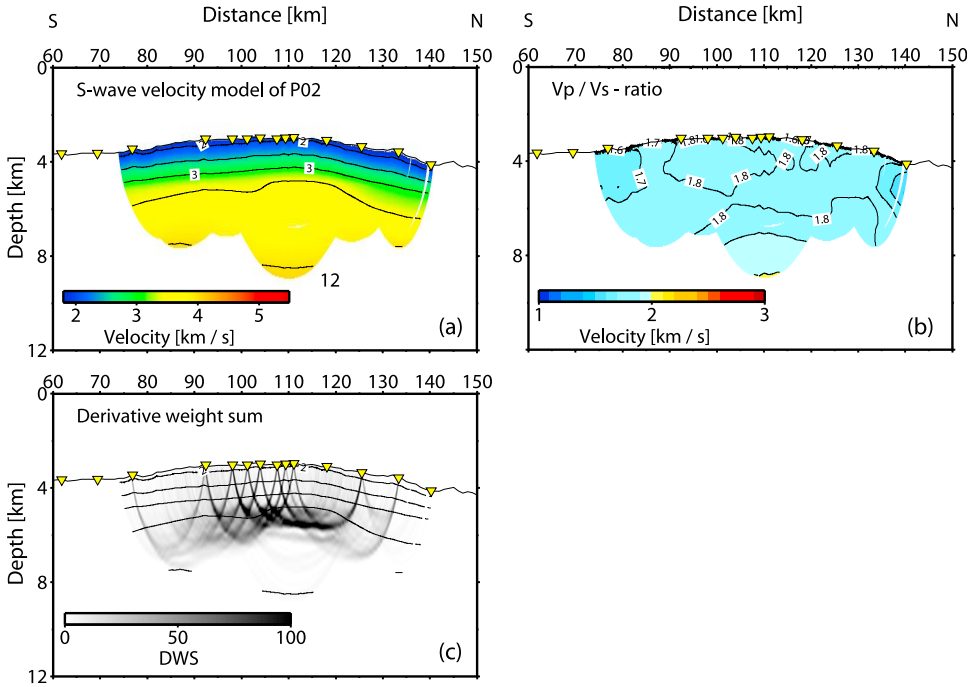

Figure 5. (a) Preferred final S wave velocity model after five iterations. The interval of the contour lines is 0.5 km/s. (b) Vp/Vs ratio of profile 2 computed by velocity grid-by-grid division of the final P and S velocity models for the first-arrival picks. (c) Resolution of the model and the ray coverage of the tomographic inversion.

corresponding approximately to the segment center. A total of 1133 S wave arrivals could be picked. After 5 iterations the model (Figure 5a) converged to a value of X^2 less than 1 with a residual traveltime misfit of 80 ms. The crustal v_P/v_S ratio is about 1.8 (Poisson's ratio of 0.28) without large variation in the central part (Figure 5b). The resolution of the v_P/v_S ratio is primarily determined by the resolution of the less well resolved S wave velocity model, as fewer and more irregularly distributed S wave traveltime data with a larger uncertainty than P wave traveltime data are available (Figure 5c).

6. Discussion

6.1. Axial Segmentation

[28] Large crustal thickness variations occur along the axis of the 90 km long TAMMAR segment. These vary from a minimum crustal thickness of

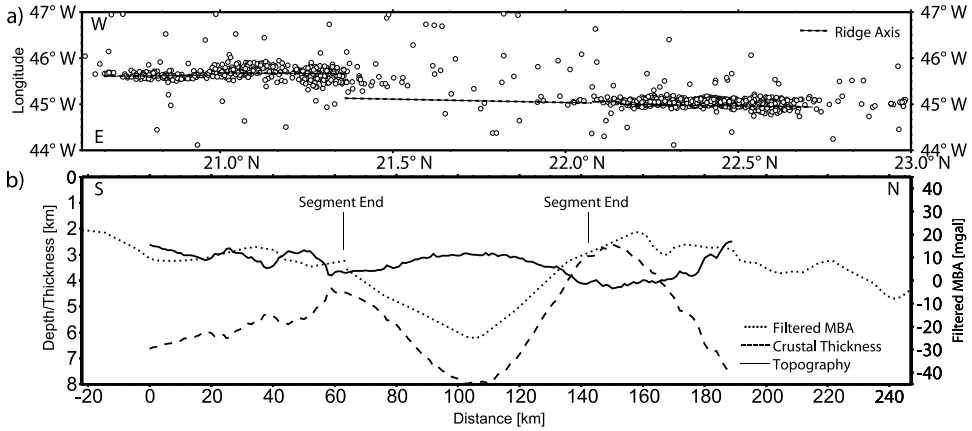

Figure 6. (a) Seismic small-scale events along the MAR. Dashed line represents the ridge axis. (b) Filtered mantle Bouguer anomaly (dotted line), topography (solid line), and crustal thickness (dashed line) of P02.

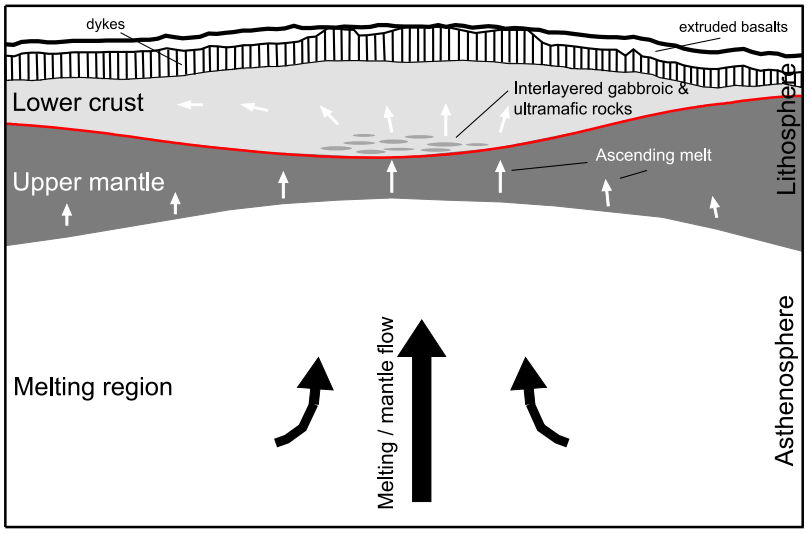

Figure 7. Sketch showing a geological interpretation of our traveltime modeling. The main features are discussed in the text.

about 4 km at the northern segment end to a maximum of about 8 km at the segment center. Toward the southern segment tip the crustal thickness decreases to about 5.5 km. Along-axis crustal thickness variations of the same order of magnitude were also inferred from the gravity-derived crustal thickness of data by *Maia and Gente* [1998], which yielded 8.5 to 9 km for the center of the segment (Figure 6). The 90 km long OH-1 segment at 35°N [*Hooft et al.*, 2000; *Canales et al.*, 2000] is of the same scale as the TAMMAR segment and has a crustal thickness of approx. 8 km at the segment center. In addition crustal thickness variation and asymmetry at the segment ends is very similar for both segments. Further, results of seismic studies at the MAR at 5°S [*Planert et al.*, 2009] and at 33°S [*Tolstoy et al.*, 1993] report on segments with a crustal thickness of about 8 to 8.5 km at the segment center and a crustal thickness variation of the same magnitude as for TAMMAR and OH-1. All those segments show similar crustal thickness in the segment center and crustal thickness variation independent on the order of the ridge axis discontinuity at their segment ends.

[29] The upper crust, seismic layer 2 at the TAMMAR segment, has a steep velocity gradient of 1.6 s^{-1} and a fairly uniform thickness of approx. 2 km. Underneath, layer 3 is marked by a small velocity gradient (less than 1 s^{-1}). The seismic velocities and gradient of layers 2 and 3 are more or less typical for young oceanic crust [*White et al.*, 1992]. The compressional wave velocity increase of layer 2 reflects the porosity of this basaltic layer rather than the melt supply [*Whitmarsh*, 1978; *Minshull et al.*, 2006]. The decrease of porosity with depth is caused by decreased pore space with depth through crack closure with increasing confining pressure.

[30] Layer 3 accommodates most of the observed crustal thickness variation. PmP arrivals are not very strong along the whole profile, however, at the ends of the segment the critical distance is very short and high velocities of about 8 km/s occur at small offsets (see for example OBH02 in Figure 2). Thus the mantle is very shallow beneath the seafloor. If this variation is interpreted as variations in melt supply, it supports strongly focused magmatic accretion beneath the segment center as proposed by *Lin et al.* [1990] by means of gravimetric data and observed for the OH-1 [*Hooft et al.*, 2000; *Canales et al.*, 2000] segment and for the segments at 5°S [*Planert et al.*, 2009] and at 33°S [*Tolstoy et al.*, 1993] using seismic data.

[31] The axial valley at the southern ridge tip is narrower compared to the northern end (Figure 1b) and the crustal thickness is larger in the south (5.5 km) compared to the northern end (4 km). Thus, the melt supply seems to be slightly higher in the south. The asymmetry between the southern ridge tip and the northern segment end in crustal thickness emphasizes that magma might be preferentially redistributed from a central injection point to the southern segment end (Figure 7), a feature perhaps related to ridge propagation. However, the thick crust in the segment center suggests that most of the melt is used locally for crustal formation. More fluid basalts might flow along axis to be

redistributed more evenly, while high-viscosity gabbroic crust tends to crystallize at the locus of rising melts.

[32] The combination of data from active and passive seismic experiments with additional gravity data gives an even better constrained model of the crustal structure. Seismic events from PMEL/NOAA's experiment [*Smith et al.*, 2003], the mantle Bouguer anomaly (MBA) [*Maia and Gente*, 1998], topography, and crustal thickness, derived from our seismic traveltime modeling, are compared in Figure 6; they display strong spatial correlations. The gap in seismic activity helps to determine the northern TAMMAR segment boundary, which is a zero-offset discontinuity. The aseismic zone may indicate thin lithosphere and comparatively hot crust under the topographic high in contrast to thicker lithosphere beneath the northern basin with reduced volcanism, comparable to the OH-1 segment [*Hooft et al.*, 2000]. The mantle Bouguer anomaly (MBA) shows a negative anomaly, indicating crustal thickening, consistent with our seismic observations that better resolve the changes in internal crustal structure.

6.2. Crustal Construction

[33] Higher upper crustal P wave velocities were observed in the central part of the TAMMAR segment compared to its tips. A plausible explanation for this is that the basalt in the segment center is more homogeneous and consolidated than at its ends. Piled lava flows are predominant in the center of the segment while pillows exist at the end (J. Dyment, personal communication, 2009). The tectonic disruption of the basaltic layer may also be more pronounced at the ends than at the center, as also expressed in the hourglass-shaped median valley.

[34] Figure 7 shows our preferred model of the internal structure of the TAMMAR segment and flow patterns in the uppermost mantle and crust. Not resolved in our velocity modeling but inferred from seafloor observations [*Gente et al.*, 1995, 1996] and magnetization [*Honsho et al.*, 2009] is that a thin layer of pillows covers the intrusive zone. In the segment center the seafloor is covered by old and young lava lakes. The thickness of the magmatic section (including seismic layers 2 and 3) of the lithosphere in the segment center may be underestimated. However, layer 3, interpreted as gabbroic rocks, thins toward the segment ends (compare to the velocity model in Figure 3a).

[35] The central part of the segment shows higher velocities at the bottom of seismic layer 3. The P wave velocity increases up to 7.4 km/s, too fast for gabbros but too slow for mantle rocks. These observed velocities in the Moho transition zone are comparable to partially serpentinized peridotites [*Christensen*, 1966]. However, it is uncertain that seawater would penetrate in a midsegment setting to that great depth to induce subaxial serpentinization. The low seismicity [*Smith et al.*, 2003] suggests a rather ductile lower crust and implies low tectonism and thus no deep fractures cutting into the lower crust or down to the mantle. The seismic Moho represents a rapid increase from crustal velocities to upper mantle velocities in excess of 8 km/s [*Purdy and Ewing*, 1986]. Connecting the seismic Moho to a change in lithology, as often done for ophiolites (Oman ophiolite [*Kelemen et al.*, 1997] and Bay of Islands ophiolite [*Karson et al.*, 1984]), we interpreted the seismic Moho as the boundary between interlayered gabbroic and ultramafic rocks and ultramafic cumulates. The petrologic Moho is the boundary between the magmatic section (e.g., base of ultramafic cumulates) and the residual depleted mantle [*Karson and Elthon*, 1987]. This zone of higher seismic velocities could be interpreted as an alternating sequence of gabbros and cumulates, or as peridotites. Similar observations were found in the OH-1 segment at 35°N [*Canales et al.*, 2000]. The seismic Moho derived by the traveltime modeling would then represent the base of this transition zone.

[36] Early works of *Orcutt et al.* [1976] and *Rosendahl et al.* [1976] provided the first observations of a seismic low-velocity zone beneath the East Pacific Rise, which led to an increased search for comparable features beneath the MAR. Along the MAR, seismic evidence for a shallow axial magma chamber (AMC) has been found in the Lucky Strike segment [*Singh et al.*, 1998, 2006] and in the southernmost part of the Reykjanes Ridge [*Navin et al.*, 1998]. Anomalously low seismic velocities are also found beneath the Snake Pit neovolcanic zone in the MARK area [*Calvert*, 1995; *Canales et al.*, 2000] with clear indications of crustal melt. *Sinha et al.* [1998] found that shallow, melt-rich AMCs at the MAR are short lived. Magma chambers at the MAR are likely to be transient, and successful seismic imaging of them at a slow spreading ridge has been difficult.

[37] Our seismic data do provide neither evidence for seismic low-velocity zones nor delayed arrivals in the seismic sections that can be associated with a crustal magma chamber comparable to the studies of *Sinha et al.* [1998], *Canales et al.* [2000], or *Menke*

et al. [2002]. Indeed, the observation of converted shear waves is incompatible with the presence of a substantial fluid magma body, since only P waves propagate through fluids. The existence of fluids significantly affects the P wave velocity in the rocks while S wave velocities are hardly affected; thus, changes in the v_p/v_s ratio would be expected. The shear wave traveltime tomography resolved the central part of the TAMMAR segment to a depth of 4 km (Figure 6). No major changes in the v_p/v_s ratio were seen in our modeling. Both, P wave velocity and S wave velocity increase gradually with depth with a ratio of about 1.8. However, the tomography method tends to underpredict low-velocity zones (as can be seen in the checkerboard test in Figure 4). Given that the resolution of the imaging is no better than 2 km, partial melt in small isolated pockets could certainly exist, and be fed by hotter and deeper melts from a magmatic system at greater depth underlying the crustal portion of the segment. The absence of strong mantle phases (Pn) in the seismic data beneath the segment center might be a hint for a hot lithosphere. The fossil lava lakes in the segment center, a rare feature on slow spreading ridges, are witnesses to recent periods with high volcanic effusion rates. A structural model from submersible magnetic data [*Honsho et al.*, 2009] shows the last magmatic highly active period was about 0.45 Ma ago lasting over 150,000 years. Thus, a subaxial lens of partial melt may have existed at certain times but be absent now.

6.3. Ridge Propagation

[38] The results of the P wave traveltime tomography show significant differences in the crustal structure within the segment and a north to south asymmetry. At the southern end of the segment seismic velocities become anomalously low compared to average MAR values. Velocities as low as 6 km/s have been found at 3 km below the seafloor. The velocity gradient reaches almost 1 s^{-1} below layer 2, which is rather high compared to average Atlantic crust. This is interpreted to be an effect of increased porosity due to fracturing caused by more intense tectonism near the segment ends. The fracturing causes crack propagation and subsequent filling by extrusive lavas, thus, lowering seismic P wave velocities. This process appears comparable to other segments along the MAR [*Hooft et al.*, 2000] and may locally be enhanced by the southward propagation of the segment and changes in the regional stress field. Changes in the stress field might be related to tectonic rotations of the crust between the propagating and the dying ridge associated with the migrated offset [*Pockalny et al.*, 1995].

[39] The earthquake distribution [*Smith et al.*, 2003; *Kahle*, 2007] supports our observations of a recently magmatically active TAMMAR segment. However, the lack of seismicity is not a reasonable phenomenon for ridge propagation. Rather it indicates the thermal state of the crust, and thus indirectly indicates magmatic activity of a ridge segment during temporal variations in a magmatic-tectonic crustal accretion cycle. The appearance of enhanced mantle upwelling seems to have coincided with the onset of propagation 4.5 million years ago as indicated by the observed Mantle Bouguer Anomaly [*Maia and Gente*, 1998]. *Kahle* [2007] suggested that spreading at the doomed ridge is taken up by mechanical rifting with minimal associated volcanism; thus, the magmatic active segment [*Gente et al.*, 1995] is propagating into the older lithosphere of a magmatically starved segment. The gravitational and thermal differences between ridge segments and the high amount of melts connected to mantle upwelling may potentially be the driving mechanism for the migration of an earlier stable fracture zone setting.

[40] The orientation of the oblique features in the bathymetry provides information about propagation rates. The TAMMAR segment is lengthening to the south and to the north. The segment center is migrating southward (Figure 1b). This prominent V-shaped wake in the bathymetry is caused by the ridge propagation into older lithosphere with an offset to the doomed ridge. The impact of the northern lengthening into a zero-offset discontinuity setting is less pronounced in the bathymetry. However, the northern termination of the ridge axis parallel abyssal hills supports this interpretation. The propagation rates are 16 mm/y in the south and 7 mm/y at the northern segment end (compare to Figure 1). The structures suggest a much slower propagation rate toward the north. This is still broadly consistent with the concept of mantle upwelling and focused melt supply as the main mechanism for ridge propagation, and would also explain reversely oriented structures like the V-shaped structure between the TAMMAR segment and the Kane fracture zone at 23°N. The propagation rate seems to be controlled by the amount of magma that reaches the segment ends. Our traveltime tomographic results (Figure 3) show a 1.5 km thicker crust at the southern segment end compared to the northern segment end. The propagation rate is 1.5 times faster compared to the north. The axial valley is wider in the north constraining that

here spreading is less well compensated by magmatic diking. Assuming focused melt supply in the segment center, a large portion is transported laterally at crustal levels, possibly through dikes toward south and a smaller part toward the north. Preferential along-axis dike propagation may be seen as a potential driving mechanism for ridge propagation. When the magma budget is reduced, propagation stops. This attends the observed propagation rate dependence on the spreading rate of a ridge segment, with a higher propagation rate where the spreading rate is higher [*Phipps Morgan and Sandwell*, 1994]. To the north a second large negative mantle Bouguer anomaly [*Gente et al.*, 1995] occurs (indicated in Figure 6) and suggests crustal thickening and hence mantle upwelling. This segment was propagating toward the north and south leaving clear oblique structures in the bathymetry at its northern segment end. The OH-1 segment at 35°N [*Hooft et al.*, 2000] represents another example of a propagating segment that was studied with seismic refraction and wide-angle reflection data. A negative mantle Bouguer anomaly coincides in shape with the trails left by the ridge propagation. Propagation started roughly 5 million years ago. At that time enhanced melt supply to the crustal region was observed at the segment center and is expressed in a seamount chain [*Rabain et al.*, 2001]. Both segments, TAMMAR and OH-1, show an asymmetry in crustal thickness at the segment ends with thicker crust at the propagating ridge tip. This emphasizes that propagation might be related to the amount of redistributed magma from a central injection point. The locus of melt supply for the TAMMAR segment has migrated southward (Figure 1b), perhaps causing the destruction of the apparently stable transform fault.

[41] Our data show no evidence for a continuous along axis shallow magma reservoir that feeds the dikes, although a discontinuous thin layer might be below the resolution. This might suggest that the dikes were fed from a lower or subcrustal reservoir near the center of the segment. The propagating ridge is seen to be virtually aseismic (at the short time scale of observation). However, small clusters of events were observed at the southern ridge tip using the seismic network deployed within the project [*Kahle*, 2007]. These events are of magnitudes smaller than M_L 2.5, and may be associated with diking. *Buck et al.* [2006] showed that the length of dikes should depend on the thickness of the lithosphere and the width of the dike. Other studies observed that dikes can reach lengths of several tens of kilometers. Dikes fed from shallow reservoirs will solidify over the time periods of propagation [*Fialko and Rubin*, 1998], however, dikes rising from greater depths and higher temperatures may cool over much longer periods, effectively maintaining an open conduit at depth [*Buck et al.*, 2006]. A higher value of magma pressure is needed to start dike propagation. Dikes penetrate in the direction of minimum tectonic stress adjacent to the magma chamber [*Buck et al.*, 2006]. This might have started roughly 5 million years ago, with a change from tectonically dominated asymmetric spreading to magmatically dominated spreading in this area. The fossil core complex on the western ridge flank north to the ancient transform (Figure 1) might be a witness of this transition its formation stopping at the onset of segment propagation. After its initiation, the magma budget appears to have remained constant. This is consistent with constant ridge propagation over millions of years after a rapid onset, occurring via diking that occurs in discrete periods. Similar to Afar [*Ebinger et al.*, 2008], the southern tip is marked by isolated volcanoes and many scarps exist at both walls of the valley [*Gente et al.*, 1996] indicating strong tectonism at the southern ridge tip. The size of the upwelling may control the evolution of ridge segments, and thus ultimately the propagation length.

6.4. Mechanisms Triggering Propagation

[42] In the introduction several mechanisms were briefly reviewed that may explain and trigger the evolution of PRs. *Brozena and White* [1990] suggested that the existence of PRs along the MAR is due to mantle flow away from hot sports. However, south of 26.5°N they point randomly to the South and to the North. Additionally, our seismic data support the interpretation of focused vertical melt delivery at the ridge axis. Thus, this model does not seem applicable to our study area. *Kleinrock and Tucholke* [1997] showed that shallow gravity stresses, caused by gravitational sliding down the along-ridge axis topographic gradient [*Phipps Morgan and Parmentier*, 1985; *Phipps Morgan and Sandwell*, 1994], cannot be related to many propagators. However, they found that initiation of fast propagators might be due to changes in the tectonic extension of seafloor spreading. We interpret our data in terms of propagation driven by enhanced melt supply. Initiation of propagation connected to enhanced melt supply was also favored at the OH-1 segment [*Hooft et al.*, 2000; *Rabain et al.*, 2001].

[43] We do not observe major changes at the transform fault at 21°40′ that may indicate reorganization of the plates roughly 4.5 ma ago, similar to the observations at the Pacific-Antarctic Ridge

(PAR) [*Wilson et al.*, 1984; *Briais et al.*, 2002]. However, as part of this study we systematically reviewed propagating segments along the MAR. We notice that intersections or ends of the inner and outer pseudofaults are close to bends in the FZs that reflect changes in the spreading direction (examples: MAR at 35°N, 25.75°N, MAR at 20°N, MAR 0°S, Chile Ridge at 44°S). These observations may indicate that propagators might be initiated by small rotation of the spreading direction. However, we could not observe propagators that initiated at the same time. Therefore, although plates behave in a rigid way at large scale, locally, they may behave in a less rigid way and respond to changes differently. Continuous propagation after a rapid initiation suggests that a combination of two distinct processes, triggering and runaway, shape propagation. For example, first the propagation is triggered by a small change in plate motion. Afterward, magmatic diking linked to segment-scale variations in focused mantle upwelling, mantle upwelling leads to a continuous phase of propagation until the propagator dies or, more commonly, runs into a ridge offset large enough to stop propagation. Mantle temperature and spreading rate variations are fundamental variables that determine the physical behavior of the upwelling and melting mantle as well as the extent of mantle melting and crustal production [*Niu et al.*, 2001].

[44] Smaller transform faults and nonrigid discontinuities are not necessarily barriers for a propagator as can be seen in our study area and several other places along spreading centers (e.g., MAR at 20°S, MAR at 45°S). A rate limiter appears to be the magmatic budget within the propagating segment that could also limit the length to which a propagator can extend. A new transform fault will form when propagation stops, linking the newly formed segment end with the end of the doomed rift [*Hey et al.*, 1988].

7. Conclusions

[45] The TAMMAR segment hosts a rapidly propagating ridge tip. Seismic data obtained along the ridge axis yielded strong lateral variations in crustal thickness of up to 4 km. Crust is with 8 km thickest in the segment center where mantle upwelling is believed to occur and thins approaching the segment ends. However, the southern ridge tip has with a 5.5 km thick crust a ~1.5 km thicker crustal layer than the northern segment end.

[46] The crustal structure emphasizes the role of mantle upwelling on shaping along-axis crustal structure, with focused melt supply in the segment center and preferential transport of melts at crustal levels toward the south in the direction of preferred ridge tip propagation. The thick crust in the segment center suggests that much of the enhanced local melt supply is consumed locally for crustal formation. This fact is illustrated by the observation that fluid basaltic melts forming the upper crust are redistributed more effectively along axis by lateral dike growth than the lower crust build up of gabbroic rocks that tend to crystallize and accrete nearer to the locus of mantle upwelling. Thus, crustal thickness variations are governed by variations in layer 3 thickness. The fastest lower crustal velocities are reached with 7.2 km/s in the segment center above the seismic Moho. This high-velocity zone is interpreted as an interlayered zone of gabbroic and ultramafic rocks.

[47] The observations suggest that the initiation of ridge propagation at the TAMMAR segment is primary controlled by the magma supply. Thus, enhanced mantle upwelling triggered the onset of ridge propagation. The TAMMAR segment did lengthen toward both the north and south. However, crustal thickness and bathymetric features indicate a much higher propagation rate toward the south. The propagation rate seems to be controlled by the amount of magma that reaches the segment ends. Further, the locus of melt supply for this segment center has also migrated southward.

[48] The appearance of focused along-axis melt supply appears to be coeval with the onset of propagation 4.5 million years ago, and might be responsible for the migration through an earlier stable fracture zone setting. Nonstable discontinuities were not barriers for these propagating segments. The size of the upwelling may control the evolution of ridge segments, and thus ultimately the propagation length.

Acknowledgments

[49] The COSTMAR experiment was funded by the Deutsche Forschungsgemeinschaft (DFG), grants Mo 961/5-1, Ra 925/5-1, and Gr 1964/8-2+8-3. The authors thank their colleagues who supported the work during the cruise and give particular thanks to the ship's master Captain Kull and the crew of R/V *Meteor*. We appreciate reviews by Emilie Hooft, an anonymous referee, and the Associate Editor.

References

Bergman, E. A., and S. C. Solomon (1990), Earthquake swarms on the Mid-Atlantic Ridge: Products of magmatism or extensional tectonics?, *J. Geophys. Res.*, *95*(B4), 4943–4965, doi:10.1029/JB095iB04p04943.

Briais, A., D. Aslanian, L. Geli, and H. Ondréas (2002), Analysis of propagators along the Pacific-Antarctic Ridge: Evidence for triggering by kinematic changes, *Earth Planet. Sci. Lett.*, *199*, 415–428, doi:10.1016/S0012-821X(02)00567-8.

Brozena, J. M., and R. S. White (1990), Ridge jumps and propagations in the South Atlantic Ocean, *Nature*, *348*, 149–152, doi:10.1038/348149a0.

Buck, W. R., P. Einarsson, and B. Brandsdóttir (2006), Tectonic stress and magma chamber size as controls on dike propagation: Constraints from the 1975–1984 Krafla rifting episode, *J. Geophys. Res.*, *111*, B12404, doi:10.1029/2005JB003879.

Calvert, A. J. (1995), Seismic evidence for a magma chamber beneath the slow-spreading Mid-Atlantic Ridge, *Nature*, *377*, 410–414, doi:10.1038/377410a0.

Canales, P., R. S. Detrick, J. Lin, and J. A. Collins (2000), Crustal and upper mantle seismic structure beneath the rift mountains and across a nontransform offset at the Mid-Atlantic Ridge (35°N), *J. Geophys. Res.*, *105*, 2699–2719, doi:10.1029/1999JB900379.

Carbotte, S., S. M. Welch, and K. C. Macdonald (1991), Spreading rates, rift propagation and fracture zone offset histories during the past 5 my on the Mid-Atlantic Ridge: 25°–27°30′S and 31°–34°S, *Mar. Geophys. Res.*, *13*, 51–80, doi:10.1007/BF02428195.

Christensen, N. I. (1966), Elasticity of ultrabasic rocks, *J. Geophys. Res.*, *71*, 5921–5931.

Cormier, M. H., and K. C. MacDonald (1994), East Pacific Rise 18°–19°S: Asymmetric spreading and ridge reorientation by ultra-fast migration of axial discontinuities, *J. Geophys. Res.*, *99*, 543–564, doi:10.1029/93JB02382.

Dannowski, A., I. Grevemeyer, C. R. Ranero, G. Ceuleneer, M. Maia, J. P. Morgan, and P. Gente (2010), Seismic structure of an oceanic core complex at the Mid-Atlantic Ridge, 22°19′N, *J. Geophys. Res.*, *115*, B07106, doi:10.1029/2009JB006943.

DeMets, D., et al. (1990), Current plate motions, *Geophys. J. Int.*, *101*, 425–478, doi:10.1111/j.1365-246X.1990.tb06579.x.

Ebinger, C. J., D. Keir, A. Ayele, E. Calais, T. J. Wright, M. Belachew, J. O. S. Hammond, E. Campbell, and W. R. Buck (2008), Capturing magma intrusion and faulting processes during continental rupture: Seismicity of the Dabbahu (Afar) rift, *Geophys. J. Int.*, *174*, 1138–1152, doi:10.1111/j.1365-246X.2008.03877.x.

Fialko, Y. A., and A. M. Rubin (1998), Thermodynamics of lateral dike propagation: Implications for crustal accretion at slow spreading mid-ocean ridges, *J. Geophys. Res.*, *103*, 2501–2514, doi:10.1029/97JB03105.

Gac, S., C. Tisseau, J. Dyment, and J. Goslin (2006), Modelling the thermal evolution of slow-spreading ridge segments and their off-axis geophysical signature, *Geophys. J. Int.*, *164*, 341–358, doi:10.1111/j.1365-246X.2005.02844.x.

Gente, P., R. Pockalny, C. Durand, M. Maia, C. Deplus, C. Mével, G. Ceuleneer, M. Cannat, and C. Laverne (1995), Characteristics and evolution of the segmentation of the Mid-Atlantic ridge between 20°N and 24°N during the last 10 million years, *Earth Planet. Sci. Lett.*, *129*, 55–71, doi:10.1016/0012-821X(94)00233-O.

Gente, P., G. Ceuleneer, O. Dauteuil, J. Dyment, C. Honsho, C. Laverne, C. LeTrudu, N. C. Mitchell, M. Ravilly, and R. Thebaud (1996), On- and off-axis submersible investigations on an highly magmatic segment of the Mid-Atlantic Ridge (21°40′N): The TAMMAR cruise, *InterRidge News*, *5*(2), 27–31.

Hey, R. N. (1977), A new class of pseudofaults and their bearing on plate tectonics: A propagating rift model, *Earth Planet. Sci. Lett.*, *37*, 321–325, doi:10.1016/0012-821X(77)90177-7.

Hey, R. N., F. K. Duennebier, and W. J. Morgan (1980), Propagating rifts on mid-ocean ridges, *J. Geophys. Res.*, *85*, 3647–3658, doi:10.1029/JB085iB07p03647.

Hey, R. N., M. C. Kleinrock, S. P. Miller, T. M. Atwater, and R. C. Searle (1986), Sea beam/deep-tow investigation of an active oceanic propagation rift system, Galapagos 95.5°W, *J. Geophys. Res.*, *91*, 3369–3393, doi:10.1029/JB091iB03p03369.

Hey, R. N., H. W. Menard, T. M. Atwater, and D. W. Caress (1988), Changes in direction of seafloor spreading revisited, *J. Geophys. Res.*, *93*, 2803–2811, doi:10.1029/JB093iB04p02803.

Honsho, C., J. Dyment, K. Tamaki, M. Ravilly, H. Horen, and P. Gente (2009), Magnetic structure of a slow spreading ridge segment: Insights from near-bottom magnetic measurements on board a submersible, *J. Geophys. Res.*, *114*, B05101, doi:10.1029/2008JB005915.

Hooft, E. E. E., R. S. Detrick, D. R. Toomey, J. A. Collins, and J. Lin (2000), Crustal thickness and structure along three contrasting spreading segments of the Mid-Atlantic Ridge (35°N), *J. Geophys. Res.*, *105*, 8205–8226, doi:10.1029/1999JB900442.

Kahle, R. L. (2007), A seismic investigation of the 21.5° N propagating segment on the Mid-Atlantic Ridge, doctor thesis, St. John's College, Univ. of Cambridge, Cambridge, U. K.

Karson, J. A., and D. Elthon (1987), Evidence for variations in magma production along oceanic spreading centres: A critical appraisal, *Geology*, *15*, 127–131, doi:10.1130/0091-7613(1987)15<127:EFVIMP>2.0.CO;2.

Karson, J. A., J. A. Collins, and J. F. Casey (1984), Geologic and seismic velocity structure of the crust/mantle transition in the Bay of Islands ophiolite complex, *J. Geophys. Res.*, *89*, 6126–6138, doi:10.1029/JB089iB07p06126.

Kelemen, P. B., K. Koga, and N. Shimizu (1997), Geochemistry of gabbro sills in the crust-mantle transition zone of the Oman ophiolite: Implications for the origin of the oceanic lower crust, *Earth Planet. Sci. Lett.*, *146*, 475–488, doi:10.1016/S0012-821X(96)00235-X.

Kleinrock, M. C., and B. E. Tucholke (1997), Fast rift propagation at a slow-spreading ridge, *Geology*, *25*, 639–642, doi:10.1130/0091-7613(1997)025<0639:FRPAAS>2.3.CO;2.

Korenaga, J., W. S. Holbrook, and T. Dahl-Jensen (2000), Crustal structure of the southeast Greenland margin from joint refraction and reflection seismic tomography, *J. Geophys. Res.*, *105*, 21,591–21,614.

Lin, J., and J. Phipps Morgan (1992), The spreading rate dependence of three-dimensional Mid-Ocean Ridge gravity structure, *Geophys. Res. Lett.*, *19*, 13–16, doi:10.1029/91GL03041.

Lin, J., G. M. Purdy, H. Schouten, J. C. Sempere, and C. Zervas (1990), Evidence from gravity data for focused magmatic accretion along the Mid-Atlantic Ridge, *Nature*, *344*, 627–632, doi:10.1038/344627a0.

MacDonald, K. C., P. J. Fox, L. J. Perram, M. F. Eisen, R. M. Haymon, S. P. Miller, S. M. Carbotte, M. H. Cormier, and A. N. Shor (1988), A new view of the mid-ocean ridge from the behavior of ridge-axis discontinuities, *Nature*, *335*, 217–225, doi:10.1038/335217a0.

MacDonald, K. C., D. S. Scheirer, and S. M. Carbotte (1991), Mid-ocean ridges: Discontinuities, segments and giant cracks, *Science*, *253*, 986–994, doi:10.1126/science.253.5023.986.

Magde, L. S., and D. W. Sparks (1997), Three-dimensional mantle upwelling, melt generation, and melt migration beneath segment slow spreading ridges, *J. Geophys. Res.*, *102*, 20,571–20,583.

Maia, M., and P. Gente (1998), Three-dimensional gravity and bathymetry analysis of the Mid-Atlantic Ridge between 20°N and 24°N: Flow geometry and temporal evolution of the segmentation, *J. Geophys. Res.*, *103*, 951–974, doi:10.1029/97JB01635.

McKenzie, D. (1986), The geometry of propagating rifts, *Earth Planet. Sci. Lett.*, *77*, 176–186, doi:10.1016/0012-821X(86)90159-7.

Menke, W., M. West, and M. Tolstoy (2002), Shallow crustal magma chamber beneath the axial high of the Coaxial Segment of Juan de Fuca Ridge at the "Source Site" of the 1993 eruption, *Geology*, *30*, 359–362, doi:10.1130/0091-7613(2002)030<0359:SCMCBT>2.0.CO;2.

Minshull, T. A., M. R. Muller, and R. S. White (2006), Crustal structure of the Southwest Indian Ridge at 66°E, *Geophys. J. Int.*, *166*, 135–147, doi:10.1111/j.1365-246X.2006.03001.x.

Moser, T. J. (1991), Shortest path calculation of seismic rays, *Geophysics*, *56*, 59–67, doi:10.1190/1.1442958.

Moser, T. J., G. Nolet, and R. Snieder (1992), Ray bending revisited, *Bull. Seismol. Soc. Am.*, *82*, 259–288.

Navin, D. A., C. Peirce, and M. C. Sinha (1998), The RAMESSES experiment—II. Evidence for accumulated melt beneath a slow spreading ridge from wide-angle refraction and multichannel reflection profiles, *Geophys. J. Int.*, *135*, 746–772, doi:10.1046/j.1365-246X.1998.00709.x.

Niu, Y., D. Bideau, R. Hékinian, and R. Batiza (2001), Mantle compositional control on the extend of mantle melting, crust production, gravity anomaly, ridge morphology, and ridge segmentation: A case study at the Mid-Atlantic Ridge 33–35°N, *Earth Planet. Sci. Lett.*, *186*, 383–399, doi:10.1016/S0012-821X(01)00255-2.

Orcutt, J. A., B. L. N. Kennett, and L. M. Dorman (1976), Structure of the East Pacific Rise from an ocean bottom seismometer survey, *Geophys. J. Int.*, *45*, 305–320, doi:10.1111/j.1365-246X.1976.tb00328.x.

Phipps Morgan, J., and E. M. Parmentier (1985), Causes and rate-limiting mechanisms of ridge propagation: A fracture mechanics model, *J. Geophys. Res.*, *90*, 8603–8612, doi:10.1029/JB090iB10p08603.

Phipps Morgan, J., and D. T. Sandwell (1994), Systematics of ridge propagation south of 30°S, *Earth Planet. Sci. Lett.*, *121*, 245–258, doi:10.1016/0012-821X(94)90043-4.

Planert, L., E. R. Flueh, and T. J. Reston (2009), Along- and across-axis variations in crustal thickness and structure at the Mid-Atlantic Ridge at 5°S obtained from wide-angle seismic tomography: Implications for ridge segmentation, *J. Geophys. Res.*, *114*, B09102, doi:10.1029/2008JB006103.

Pockalny, R. A., A. Smith, and P. Gente (1995), Spatial and temporal variability of crustal magnetization of a slowly spreading ridge: Mid-Atlantic Ridge (20°–24° N), *Mar. Geophys. Res.*, *17*, 301–320, doi:10.1007/BF01203467.

Purdy, G. M., and J. Ewing (1986), Seismic structure of the ocean crust, in *The Geology of North America*, vol. M, *The Western North Atlantic Region*, pp. 313–330, Geol. Soc. of Am., Boulder, Colo.

Rabain, A., M. Cannat, J. Escartin, G. Pouliquen, C. Deplus, and C. Rommevaus-Jestin (2001), Focused volcanism and growth of a slow spreading segment (Mid-Atlantic Ridge, 35°N), *Earth Planet. Sci. Lett.*, *185*, 211–224, doi:10.1016/S0012-821X(00)00371-X.

Rosendahl, B. R., R. W. Raitt, L. M. Dorman, L. D. Bibee, D. M. Hussong, and G. H. Sutton (1976), Evolution of oceanic crust: 1. A physical model of the East Pacific Rise crest derived from seismic refraction data, *J. Geophys. Res.*, *81*, 5294–5304, doi:10.1029/JB081i029p05294.

Sandwell, D. T., and W. H. F. Smith (1997), Marine gravity anomaly from Geosat and ERS-1 satellite altimetry, *J. Geophys. Res.*, *102*, 10,039–10,054, doi:10.1029/96JB03223.

Schouten, H., H. J. B. Dick, and K. D. Klitgord (1987), Migration of mid-ocean ridge volcanic segments, *Nature*, *326*, 835–839, doi:10.1038/326835a0.

Sempéré, J. C., J. Lin, H. S. Brown, H. Shouten, and G. M. Purdy (1993), Segmentation and morphotectonic variations along a slow-spreading center: Mid-Atlantic Ridge (24°00′N–30°40′N), *Mar. Geophys. Res.*, *15*, 153–200, doi:10.1007/BF01204232.

Sempéré, J. C., P. Blondel, A. Briais, T. Fujiwara, L. Géli, N. Isezaki, J. F. Pariso, L. Parson, P. Patriat, and C. Rommevaux (1995), The Mid-Atlantic Ridge between 29°N and 31°30′N in the last 10 Ma, *Earth Planet. Sci. Lett.*, *130*, 45–55, doi:10.1016/0012-821X(94)00259-2.

Singh, S. C., G. M. Kent, J. S. Collier, A. J. Harding, and J. A. Orcutt (1998), Melt to mush variations in crustal magma properties along the ridge crest at the southern East Pacific Rise, *Nature*, *394*, 874–878, doi:10.1038/29740.

Singh, S. C., W. C. Crawford, H. Carton, T. Seher, V. Combier, M. Cannat, J. P. Canales, D. Düsünür, J. Escartin, and J. M. Miranda (2006), Discovery of a magma chamber and faults beneath a Mid-Atlantic Ridge hydrothermal field, *Nature*, *442*, 1029–1032, doi:10.1038/nature05105.

Sinha, M. C., C. Constable, C. Peirce, A. White, G. Heinson, L. M. MacGregor, and D. A. Navin (1998), Magmatic processes at slow spreading ridges: Implications of the RAMESSES experiment at 57°45′N on the Mid-Atlantic Ridge, *Geophys. J. Int.*, *135*, 731–745, doi:10.1046/j.1365-246X.1998.00704.x.

Smith, D. K., J. Escartin, M. Cannat, M. Tolstoy, C. G. Fox, D. R. Bohnenstiel, and S. Basin (2003), Spatial and temporal distribution of seismicity along the Mid-Atlantic Ridge (15–35°N), *J. Geophys. Res.*, *108*(B3), 2167, doi:10.1029/2002JB001964.

Thibaud, R., P. Gente, and M. Maia (1998), A systematic analysis of the Mid-Atlantic Ridge morphology and gravity between 15°N and 40°N: Constraints of the thermal structure, *J. Geophys. Res.*, *103*(B10), 24,223–24,243.

Tolstoy, M., A. J. Harding, and J. A. Orcutt (1993), Crustal thickness on the Mid-Atlantic Ridge: Bull's-eye gravity anomalies and focussed accretion, *Science*, *262*(5134), 726–729, doi:10.1126/science.262.5134.726.

White, R. S., D. McKenzie, and R. K. O'Nions (1992), Oceanic crustal thickness from seismic measurements and rare earth element inversions, *J. Geophys. Res.*, *97*, 19,683–19,715, doi:10.1029/92JB01749.

Whitmarsh, R. B. (1978), Seismic refraction studies of the upper igneous crust in the North Atlantic and porosity estimates for Layer 2, *Earth Planet. Sci. Lett.*, *37*, 451–464, doi:10.1016/0012-821X(78)90061-4.

Wilson, D. S., R. N. Hey, and C. Nishimura (1984), Propagation as a mechanism of reorientation of the Juan de Fuca Ridge, *J. Geophys. Res.*, *89*, 9215–9225, doi:10.1029/JB089iB11p09215.